THE JOURNAL OF PHYSICAL CHEMISTRY C
A JOURNAL OF THE AMERICAN CHEMICAL SOCIETY

pubs.acs.org/JPCC

Article

Importance of Pd Distribution to Au−Pd Nanocrystals with High Refractive Index Sensitivity

Zachary J. Woessner, Alexander N. Chen, and Sara E. Skrabalak*

Cite This: *J. Phys. Chem. C* 2021, 125, 11262−11270

Read Online

ACCESS | Metrics & More | Article Recommendations | Supporting Information

ABSTRACT: Plasmonic metal nanoparticles (NPs) show promise in a variety of applications, ranging from theranostics to chemical sensing, with chemical sensing made possible by the sensitivity of the localized surface plasmon resonance (LSPR) to the surrounding dielectric environment. Au NPs have been the standard for LSPR sensing applications due to their narrow plasmon band, tunable LSPR maximum, and relative chemical stability; however, the comparatively low refractive index sensitivity (RIS) and morphological instability of Au nanostructures are limiting factors. Recent research has found that incorporating Pd into Au systems can increase RIS and impart multifunctionality, but how the distribution of Pd within Au-based nanostructures affects LSPR sensing is unclear. Here, Au−Pd heterostructures with different Au−Pd distributions were prepared to systematically study the effect of Pd distribution on RIS. Specifically, symmetrically branched Au nanocrystals with O_h symmetry (*i.e.*, octopods) were selected as building blocks as their branch tips concentrate E-fields locally. Using these nanocrystals as seeds, Pd-tipped Au octopods and core@shell Au@Pd octopods were synthesized for comparison to alloy Au−Pd octopods and all-Au octopods. Through experiment and simulation, we show that RIS depends both on Pd loading and location in Au−Pd heterostructures, with the Pd-tipped Au octopods displaying the highest RIS while maintaining a moderate figure of merit. This systematic analysis highlights that localization of Pd at LSPR hotspots is critical to achieving the highest RIS, with this insight intended to guide design of future LSPR sensors that move beyond the all-Au standard.

INTRODUCTION

Plasmonic nanoparticles (NPs), with their tunable light scattering and absorption properties, are of interest in chemical sensing, nanomedicine, and energy conversion platforms.[1−7] When a surface plasmon is confined to the nanoscale, the coherent oscillation of conduction electrons becomes localized and resonates at a specific energy.[1,3] This energy and corresponding linewidth of the localized surface plasmon resonance (LSPR) depend on NP size, shape, composition, and surroundings.[3] This dependence on NP surroundings motivates the development of LSPR sensors, where a shift in the LSPR maximum can be detected when the environment of a NP changes.[1,3] Traditionally, Au or Ag NPs have been used for LSPR sensors as their LSPRs occur in the visible region and both materials give narrow plasmon bands.[1,7] However, these materials have limitations, including the structural instability of Au and Ag nanostructures and the chemical instability (*i.e.*, oxidation) of Ag.

To mitigate these limitations, integrating metals such as Pd or Pt into Ag or Au nanostructures has gained interest.[8−12] Initially, much of this interest stemmed from the catalytic properties of Pd and Pt, and the promise of plasmon-mediated catalysis, with Pd or Pt being viewed as poor plasmonic metals themselves.[10,11] This perspective has shifted in the case of Pd on account of its high thermal stability relative to Au and Ag and the low spectral dispersion of the real component of the Pd dielectric function compared to Au and Ag across the visible spectrum.[11] This low spectral dispersion is promising for LSPR sensing applications, where refractive index sensitivity (RIS), defined as the shift in LSPR maximum per change in refractive index (RI), is the primary metric.[11] However, this feature is not generally exploited by all-Pd structures as the large imaginary component of the Pd dielectric results in significant plasmon damping.[11] To compensate, Pd can be added to a plasmonic material with a narrow and tunable LSPR, for example, Au NPs.[8,10] In this way, the benefits of each metal are integrated into one NP platform while minimizing their disadvantages. For example, previous work in our group showed the promise of alloyed AuPd octopods (eight-branched nanocrystals with O_h symmetry) as plasmonic sensors, boasting a RIS as high as 556 nm/RIU with an LSPR in the visible region.[9] Building from this achievement, we hypothesized that how Pd was integrated with Au would affect the LSPR sensing properties. Specifically, a distinction between alloying and segregated phases is needed as alloying Pd with Au leads to significant line broadening.[13] However, how the Pd spatial distribution in different heterostructures will affect LSPR sensing properties

Received: March 31, 2021
Revised: April 28, 2021
Published: May 12, 2021

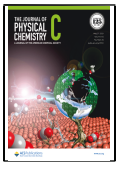

https://doi.org/10.1021/acs.jpcc.1c02907
J. Phys. Chem. C 2021, 125, 11262−11270

remains unclear. With this in mind, we further hypothesized that positioning Pd at the hotspots of individual nanocrystals would provide the greatest RIS while minimizing LSPR broadening.

To test this hypothesis, all-Au octopods were selected as building blocks to Au−Pd heterostructures as their branch tips concentrate E-fields locally. Using these nanocrystals as seeds, Pd-tipped Au octopods and core@shell Au@Pd octopods were synthesized for comparison to alloyed AuPd octopods and all-Au octopods. Experimental measurements of RIS are complemented with finite-difference time-domain (FDTD) simulations to gain insights into how both Pd loading and distribution contribute to the RIS of the various nanocrystals. As will be shown, localization of Pd at the hotspots provides the greatest benefits in terms of maximizing RIS while limiting LSPR broadening, providing a guidepost for designing future plasmonic sensors with enhanced properties.

MATERIALS AND METHODS

Materials. Chloroauric acid ($HAuCl_4 \cdot 3H_2O$, >99.9%), hexadecyltrimethylammonium bromide (CTAB, BioUltra, >99.5%), cetyltrimethylammonium chloride solution (CTAC, 0.78125 M), L-ascorbic acid (L-AA, 99%), trisodium citrate (>99%), and Pd(II) chloride ($PdCl_2$, 99.98%) were purchased from Sigma-Aldrich. Sodium bromide (NaBr, 99.50%) and dimethyl sulfoxide (DMSO, ACS reagent grade) were purchased from J.T. Baker. Poly(styrene sulfonic acid) sodium salt (Na−PSSA, MW 70,000) was purchased from Alfa Aesar. Hydrochloric acid (1 M) was purchased from Mallinckrodt. Hydrogen tetrachloropalladate (H_2PdCl_4, 10 mM) was synthesized through the dissolution of Pd(II) chloride in 20 mM hydrochloric acid under mild heat and stirring. Nanopure water (18.2 MΩ·cm) was used for every experiment.

Synthesis of Small Au Octahedra as Seeds for Au Cubes. A modified literature procedure for the synthesis of Au octahedra was used.[14] Briefly, 250 μL of $HAuCl_4$ (10 mM) aqueous solution was mixed through inversion of the capped reaction vial with 8.2 mL of nanopure water and 1.5 mL of CTAB (100 mM). Then, 120 μL of trisodium citrate (100 mM) was added and mixed through inversion. The vial was then placed in a 110 °C oil bath overnight. Particles were collected through centrifugation (8000 rpm, 15 min) and were then redispersed in 3 mL of nanopure water. The seed concentration was then standardized such that a 10:1 dilution of the NPs had an absorbance at 400 nm (A_{400}) of 0.14.

Synthesis of Au Cubes. To a 30 mL reaction vial containing 21.4 mL of nanopure water, 100 μL of $HAuCl_4$ (100 mM) and 2 mL of CTAB (200 mM) aqueous solutions were added and mixed through inversion of the capped reaction vial. Then, 1.5 mL of freshly prepared L-AA (100 mM) solution was added and mixed through inversion. Directly after, 1.0 mL of small Au seeds (see above) was added and mixed through inversion. The vial was placed in a 25 °C oil bath overnight. Particles were collected *via* centrifugation (8000 rpm, 15 min) and were then redispersed in 3 mL of nanopure water. See Table S1 for additional details concerning A_{400} standardization and seed volume change for the synthesis of smaller cubes.

Synthesis of Au Octopods. A modified literature synthesis was used.[15] Briefly, 275 μL of $HAuCl_4$ (100 mM), 2.5 mL of NaBr (50 mM), and 2.0 mL of CTAC (200 mM) aqueous solutions were added to a 30 mL reaction vial, diluted to 23.5 mL with nanopure water, and mixed through inversion of the capped reaction vial. Then, 1.5 mL of freshly prepared L-AA (100 mM) aqueous solution was added and mixed through inversion. Directly after, 1.0 mL of Au cube seeds was added followed by mixing through inversion (see Table S1 for specifics on seeds used). The vial was then placed in a 25 °C oil bath for 2.5 h. Particles were then collected *via* centrifugation (3900 rpm, 30 min) and redispersed in 3 mL of nanopure water.

Synthesis of Pd-Tipped Au Octopods. For specific samples, experimental details can be found in Table S2. In a typical synthesis, 19.9 mL of nanopure water, 100 μL of H_2PdCl_4 (10 mM), 2.0 mL of CTAC (200 mM), and 2.0 mL of trisodium citrate (100 mM) were added to a 30 mL reaction vial and mixed through inversion. Then, 1.5 mL of freshly prepared L-AA (100 mM) was added and mixed through inversion of the capped reaction vial. Directly after, 1.0 mL of Au octopod seeds was added and mixed through inversion. The vials were added to a 25 °C oil bath for 4 h after which particles were collected *via* centrifugation (3900 rpm, 30 min) and redispersed in 3 mL of nanopure water.

Synthesis of Au@Pd Octopods. For specific samples, experimental details can be found in Table S2. In a typical synthesis, 21.9 mL of nanopure water, 100 μL of H_2PdCl_4 (10 mM), and 2.0 mL of CTAB (200 mM) were added in a 30 mL reaction vial and mixed through inversion. Then, 1.5 mL of freshly prepared L-AA (100 mM) was added and mixed through inversion. Directly after, 1.0 mL of Au octopod seeds was added and mixed through inversion. The vials were added to a 25 °C oil bath for 4 h after which particles were collected *via* centrifugation (3900 rpm, 30 min) and redispersed in 3 mL of nanopure water.

RIS Experiments. Water/DMSO mixtures ranging from 0% v/v DMSO to 100% DMSO at 20% intervals were used to change the RI experienced by the Au octopods and Au−Pd heterostructures analyzed. The RI of the mixtures was calculated using the Lorentz−Lorenz model

$$\frac{(n_{12})^2 - 1}{(n_{12})^2 + 2} = \frac{\phi_1((n_1)^2 - 1)}{(n_1)^2 + 2} + \frac{\phi_2((n_2)^2 - 1)}{(n_2)^2 + 2}$$

where n_{12} is the RI of the mixture, n_1 is the RI of water (1.3334), n_2 is the RI of DMSO (1.4772), and φ_1 and φ_2 are the volume fractions of water and DMSO, respectively. To ensure colloidal stability, NPs were dispersed in 12 mL of 2 mg/mL poly(styrene sulfonic acid) sodium salt aqueous solution, concentrated *via* centrifugation and then dispersed to 2 mL of Na−PSSA aqueous solution. 100 μL aliquots of this solution were dispersed in 1 mL of the desired water/DMSO mixture (0% v/v DMSO, 20, 40, 60, 80, and 100%), and the LSPR of the NPs were measured by UV−visible spectroscopy. The concentration of Na−PSSA was kept constant in all cases to keep the impact on the mixture of the NP and water/DMSO constant. The RI of Na−PSSA is 1.3875 RIU at 20 °C.[16] The figure of merit (FOM) was calculated by dividing the RIS of the NPs by the full width at half-maximum (FWHM) of the LSPR.

FDTD Simulations. FDTD simulations were conducted using the Lumerical software. Octopod models were created using Blender software, where the initial Au octopod model had a face diagonal length of 100 nm, branch width of 50 nm, and a tip width of 18 nm (Figure S1). Pd islands were added to the model by randomly distributing 5 nm spheres around a branch tip and then copying their distribution to the remaining

https://doi.org/10.1021/acs.jpcc.1c02907
J. Phys. Chem. C 2021, 125, 11262−11270

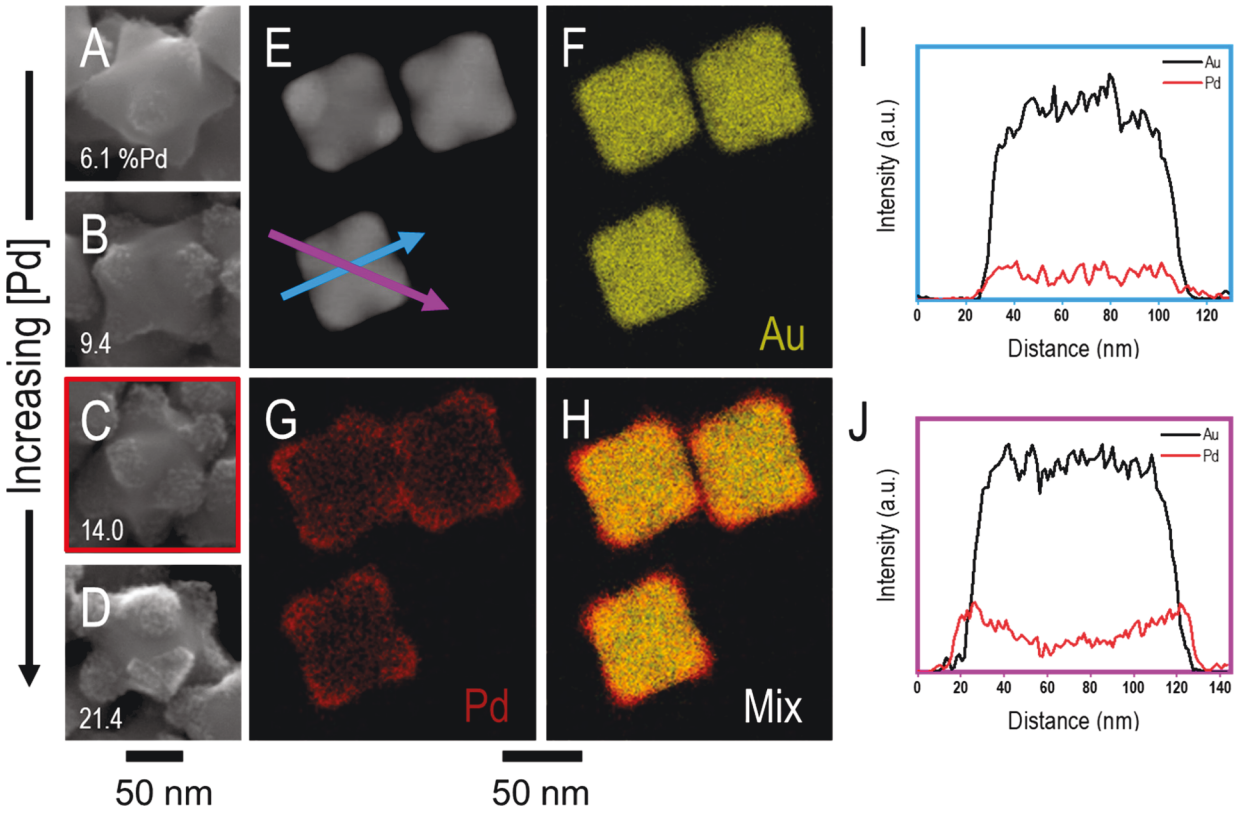

Figure 1. (A–D) Representative SEM images of Pd-tipped Au octopods with different Pd loadings determined through SEM–EDS with increasing atomic percent Pd denoted in A–D. (E) STEM and (F–H) STEM–EDS elemental mapping of sample C with Au shown in yellow (F), Pd shown in red (G), and the overlay of the two (H). (I,J) Plots of line scan analysis following the arrows in E from left to right with the blue arrow (I) and the magenta arrow (J) indicating tip localization of Pd.

branch tips. The dome-like arrangement of the spheres was achieved through placing the sphere centroid in contact with the seed mesh. The loadings were calculated through a difference in mesh volume before and after Pd addition. The volumes were then converted to mole values to get a percent Pd. The Au model was assigned a mesh priority of 1, and the Pd additions were assigned a mesh priority of 2 for the simulations. The dielectric function for Au was fitted to optical data from Johnson and Christy.[17] The dielectric function for Pd was fitted to optical data from Palik.[18] The RI of the background medium varied between 1.3334 and 1.4772 to simulate water and DMSO which were used in the experimental determination of RIS. The excitation source was a plane wave with the wavelength range of 300–1000 nm, which propagated through a surrounding medium with a RI varied between 1.3334 and 1.4772. Mesh values were set to (1 nm)^3 to calculate the scattering. The propagation direction was along the C_4 axis of the octopod.

Characterization Methods. Scanning electron microscopy (SEM) images were collected on an FEI Quanta 600F environmental SEM and a Zeiss Auriga focused-ion beam (FIB) in the SEM mode, both at a beam energy of 30 kV with a spot size of 3 μm. Transmission electron microscopy (TEM) images were collected on a JEOL 3200FS TEM operating at 300 kV with a spot size of 1. Energy-dispersive X-ray spectroscopy (EDS) was collected using an Oxford Inca dispersive X-ray system interfaced to the JEOL 3200FS TEM operating at 300 kV in the scanning TEM (STEM) mode for single particle elemental analysis. For SEM–EDS, the Oxford Inca dispersive X-ray system was interfaced to the Zeiss Auriga FIB in the SEM mode for bulk elemental analysis of micron-sized regions containing many NPs. UV–visible spectroscopy for LSPR measurements was conducted on a Varian Cary 100 Bio UV–visible spectrometer with a scan rate of 600 nm/min over the wavelength range of 200–900 nm. Dynamic light scattering (DLS) of a prepared solution was collected using the Malvern Zetasizer Nano ZS instrument at 25 °C. Measurements were carried out in triplicate to verify results. SEM samples were prepared by drop-casting a colloidal suspension (approx. 2 μL solution) on a Si wafer followed by washing with methanol after initial solvent evaporation. TEM samples were prepared by drop-casting about 2 μL of colloidal particles onto a chloroform-washed carbon-coated copper grid (to remove formvar) and then washing samples with acetone after initial solvent evaporation. Particle measurements were conducted using ImageJ software and taking the mean size of 150 particles.

RESULTS AND DISCUSSION

Spatially Selective Deposition. Au octopods were synthesized and used as seeds upon which Pd deposition occurred. Either Pd-tipped Au octopods or core@shell Au@Pd octopods were synthesized depending on the specific deposition conditions. Selective deposition of Pd was achieved by reducing H_2PdCl_4 with L-AA in the presence of the octopodal Au seeds of different sizes (Figure S2; tip-to-tip distances of 164.9 ± 5.6, 125.5 ± 4.3, 100.6 ± 2.4, 85.9 ± 2.8, 65.5 ± 2.5 nm *etc.*) in either CTAB or a mixture of CTAC and trisodium citrate.

https://doi.org/10.1021/acs.jpcc.1c02907
J. Phys. Chem. C 2021, 125, 11262–11270

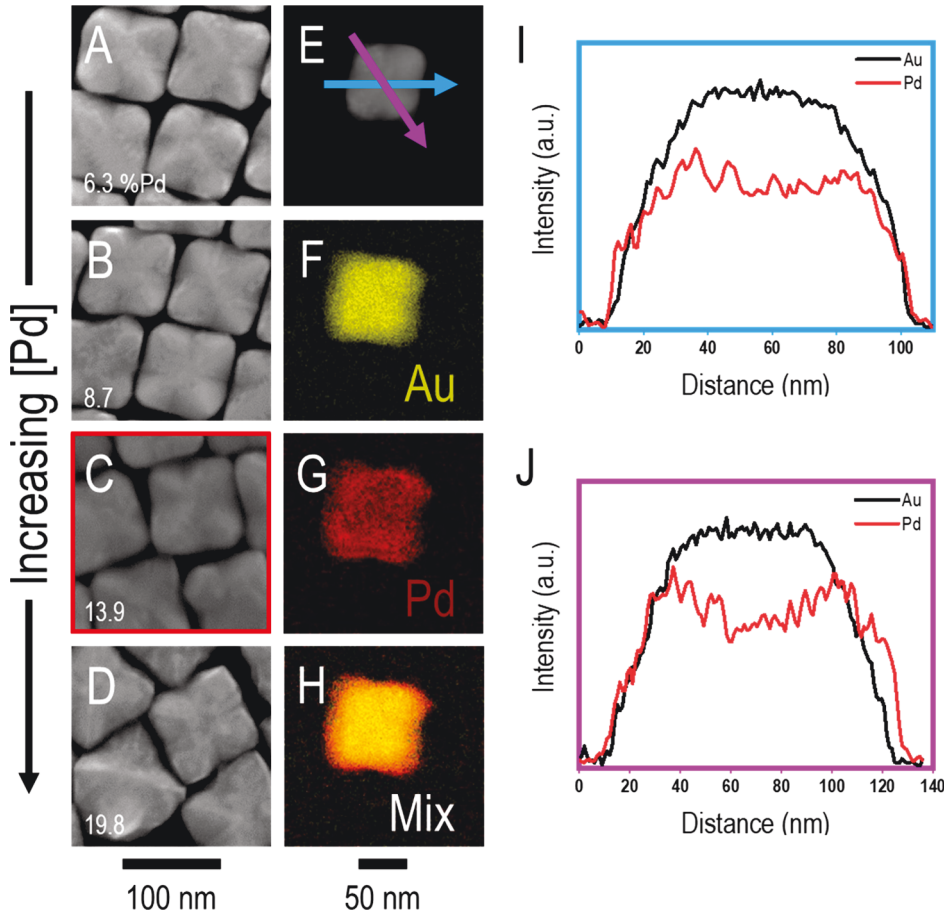

Figure 2. (A–D) Representative SEM images of Au@Pd octopods with different Pd loadings determined through SEM–EDS with increasing atomic percent Pd loading denoted in A–D. (E) STEM and (F–H) STEM–EDS elemental mapping of sample C with Au shown in yellow (F), Pd shown in red (G), and the overlay of the two (H). (I,J) Plots of line scan analysis following the arrows from left to right with the blue arrow (I) and the magenta arrow (J) in E indicating core@shell architecture.

When the Pd precursor was reduced in the presence of CTAC and trisodium citrate, islands were noted on the branch tips of the octopodal Au seeds. Holding the size of the octopodal Au seeds constant (100.6 ± 2.4 nm), the number of islands increased with increasing Pd precursor concentration (Figure 1A–D), which was concomitant with an increase in the Pd content from 6.1 to 21.4 at. % Pd, as determined by SEM–EDS. Characterization of a Pd-tipped Au octopod of intermediate Pd loading (14.0 at. % Pd; Figure 1C) with STEM–EDS further supports that the island features are Pd (Figure 1E–H). Elemental mapping data shows Pd localization toward the branch tips of the octopods. Line scan analysis for the concave regions of a particle (cyan arrow) shows a low Pd signal between the branches (Figure 1I). However, line scan analysis from tip-to-tip (magenta arrow) shows an increase in the Pd signal beyond where the Au signal is confined (Figure 1J). These data support the Pd-tipped Au octopod architecture.

In contrast, the use of CTAB produced core@shell Au@Pd octopods. This architecture is supported by the smooth nanocrystal surfaces (Figure 2A–D), with Pd loadings increasing from 6.3 to 19.8 at. % Pd with increasing Pd precursor concentrations, as determined by SEM–EDS. STEM–EDS elemental mapping of the sample with 13.9 at. % Pd (Figure 2C) shows a more even distribution of Pd than that in the CTAC/citrate system (Figure 2E–H), where the Pd signal is evenly distributed across the exterior of the surface as evident in the overlaid image (Figure 2H). Line scan analysis for the concave regions of a particle (cyan arrow) shows that the Pd signal extends past where the Au signal is observed, supporting that Pd is on the surface in between the branches (Figure 2I). Likewise, line scan analysis from tip-to-tip (magenta arrow) shows that the Pd signal again extends past the Au signal (Figure 2J), supporting the core@shell architecture.

The difference in architectures between the CTAC/citrate system (Figure 1) and the CTAB system (Figure 2) becomes clear when considering how these different reaction conditions influence the rate of deposition (V_{dep}) and the rate of diffusion (V_{diff}) of Pd adatoms. The difference in reaction conditions leads to different Pd precursor species. In the CTAB case, ligand exchange occurs where the chloride in the Pd complex is replaced by the softer bromide ions, likely leading to a $PdBr_4^{2-}$ precursor in solution.[19,20] In the CTAC/citrate case, the Pd complex remains as $PdCl_4^{2-}$. The difference in Pd precursor coordination leads to the bromide complex in the CTAB system having a more negative reduction potential, and thus a slower V_{dep}, than the chloride complex counterpart in the CTAC/citrate system.[20,21] The slower V_{dep} in the CTAB system allows for more facile diffusion to occur, yielding Au@Pd octopods. The faster reduction of the chloride complex leads to the CTAC/citrate system having a fast V_{dep} compared

https://doi.org/10.1021/acs.jpcc.1c02907
J. Phys. Chem. C 2021, 125, 11262–11270

to V_{diff}, leading to heterogeneous nucleation at the higher energy sites of the branch tips. The island-like features in the CTAC/citrate system are due to the high-energy barrier for Pd diffusion on Au in addition to the fast V_{dep}.[8] In addition, citrate is crucial for Pd-tipped Au octopod formation without simultaneous homogeneous nucleation of discrete Pd NPs, as seen in Figure S3. We hypothesize that CTAC and citrate compete for binding sites at the octopod surface, likely disrupting the CTAC bilayer and improving adatom access to the surface. In the absence of citrate, the intact CTAC bilayer may passivate too much of the surface while still favoring fast precursor reduction, resulting in homogeneous nucleation.

Both the Pd-tipped Au octopods and Au@Pd octopods can be synthesized from octopodal Au seeds of different sizes (Figure S2). When the Au−Pd ratio of seed to precursor is held constant at approximately 4:1 (20 at. % Pd), Pd-tipped Au octopods form at each size of the octopodal seed in the case of the CTAC/citrate system (Figure 3A−D), where the Pd

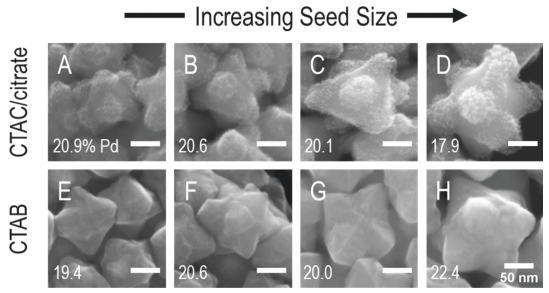

Figure 3. SEM images of Au−Pd heterostructures grown from a variety of seed sizes showing a consistency of the growth mode in the (A−D) CTAC/citrate and (E−H) CTAB systems. For each system, the inset numbers correspond to the atomic percent Pd loading confirmed through SEM−EDS. Scale bars indicate 50 nm throughout.

islands remain at and around the branch tip with approximately 20 at. % Pd loading. Similarly, Au@Pd octopods are produced in the CTAB system for each seed size examined (Figure 3E−H), again with approximately 20 at. % Pd loading. This generalizability is important due to the size- and composition-dependent optoelectronic properties displayed by plasmonic NPs, leading to a wide range of accessible wavelengths that will be discussed later.[1,3,7,11,14,22]

Optical Properties. The low spectral dispersion of Pd has shown the material to be promising for plasmonic sensing applications; however, the Pd is often coupled with Au on account of Pd having a large imaginary component of the dielectric function, leading to a broad LSPR.[11] Despite the examples that highlight the benefits of Au−Pd nanostructures, the importance of Pd location within a given nanostructure has not been systematically evaluated in the context of LSPR sensors. As such, the optical properties of the octopodal Au seeds were compared to those of Pd-tipped Au octopods and Au@Pd octopods. Specifically, the Au octopods, Pd-tipped Au octopods, and Au@Pd octopods were stabilized with Na−PSSA to ensure colloidal stability (see Figure S4 for DLS of the ∼20 at. % Pd-tipped Au octopods in water and DMSO). The LSPRs for Au octopods (tip-to-tip: 100.6 ± 2.4 nm) dispersed in water (RI = 1.3334) were compared to Pd-tipped Au octopods with approximately 10 and 20 at. % Pd loading and Au@Pd octopods with approximately 10 and 20 at. % Pd loading (Figures S5 and S6; all prepared from octopodal Au seeds with tip-to-tip: 100.6 ± 2.4 nm). As summarized in Table 1, addition of Pd leads to a red shift in LSPR maximum relative to the all-Au octopodal seeds, with the Pd-tipped Au octopods having a greater red shift than the Au@Pd octopods. Considering the Pd-tipped Au octopods, the NPs with ∼20 at. % Pd loading had a further red-shifted LSPR compared to those with ∼10 at. % Pd loading; this increase in Pd loading is coupled with broadening of the plasmon band. Considering the Au@Pd octopods, a slight blue shift of 3 nm in the LSPR maximum is observed with increasing Pd loading from 8.6 at. % Pd to 19.4 at. % Pd on to Au octopods, and broadening of the plasmon band is also observed. Such broadening with Pd addition is consistent with the large imaginary component of the Pd dielectric function compared to Au.

The RIS was determined for the same Na−PSSA-stabilized NPs built from Au octopods with tip-to-tip distance of 100.6 ± 2.4 nm by obtaining their UV−visible spectra when dispersed in various water/DMSO solutions and plotting the LSPR maximum shift as a function of the solution RI for each NP type. The results are summarized in Table 1. The Au octopods produced a moderate RIS of 275 nm/RIU with a narrow LSPR with a FWHM of 132 nm (Figure 4A, full spectra Figure S7). Notably, the Pd-tipped Au octopods with 20.6 at. % Pd loading gave not only the highest RIS of 409 nm/RIU, the most red-shifted LSPR of up to an 84 nm shift, but also the broadest LSPR with a FWHM of 240 nm (Figure 4B, full spectra Figure S7). On the other hand, Au@Pd octopods had the lowest RIS ranging from 235 to 244 nm/RIU, a slight red shift of 9−12 nm, and a broader LSPR than the Au octopods ranging from 176 to 204 nm FWHM (Figure 4C). Considering RIS as the primary metric, the Pd-tipped Au octopods with 20.6 at. % Pd loading provided the greatest RIS (Figure 4C), highlighting the importance of Pd localization at the branch tips. However, linewidth is an important metric in LSPR sensing, particularly

Table 1. Structure, Composition, and Optical Properties of Samples Highlighted in Figure 4[a]

seed size (nm)	growth mode	Pd loading (at. %)	RIS (nm/RIU)	FWHM (nm)	FOM (RIU^{-1})	λ_0 (nm)	figure location
100.6	Au	0	275	132	2.08	610	S5A
100.6	Pd-tip	20.6 (1.3)	409	240	1.71	694	S5C
100.6	Pd-tip	11.6 (0.3)	280	198	1.41	660	S5B
100.6	Au@Pd	19.4 (1.7)	244	204	1.20	619	S5E
100.6	Au@Pd	8.6 (0.5)	235	176	1.34	622	S5D
NP size (nm)	growth mode	source	RIS (nm/RIU)	FWHM (nm)	FOM (RIU^{-1})	λ_0 (nm)	reference location
95	alloy	ref 9	271	391	0.69	674	1C
105	alloy	ref 9	351	292	1.20	658	1D
118	alloy	ref 9	392	263	1.49	707	1E

[a]Numbers in parentheses represent 1 standard deviation. These structures were made using a similar protocol, as found in Figures 1 and 2.

https://doi.org/10.1021/acs.jpcc.1c02907
J. Phys. Chem. C 2021, 125, 11262−11270

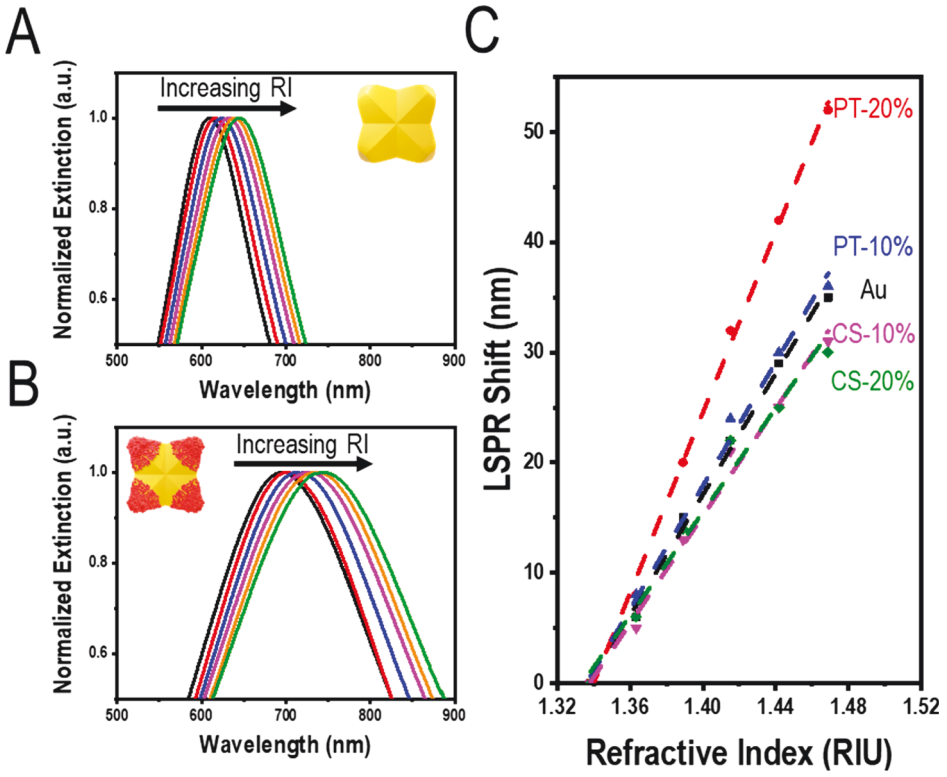

Figure 4. (A) Plot of the LSPR of the 100.6 nm all-Au octopods suspended in various mixtures of water and DMSO and (B) plot of the LSPR of 20.6 at. % Pd Pd-tipped Au octopods built from 100.6 nm seeds in various mixtures of water and DMSO. In both (A,B), the calculated RI of the mixtures, from left to right, are 1.3382, 1.3634, 1.3890, 1.4151, 1.4417, and 1.4688. (C) Plot of LSPR shift *vs* RI for the (black trace) all-Au, (red trace) 20.6% Pd-tipped Au octopods, (blue trace) 11.6% Pd-tipped Au octopods, (green trace) 19.4% Au@Pd octopods, and (magenta trace) 8.6% Au@Pd octopods. At. % Pd confirmed through SEM−EDS.

when considering multiplexing.[3] To account for linewidth, a FOM is used which divides the RIS by the LSPR FWHM. The all-Au octopods have the highest FOM (2.08 RIU^{-1}), but the Pd-tipped Au octopods with 20.6 at. % Pd loading had the second highest FOM (1.71 RIU^{-1}). Considering that the Au@Pd octopods with similar Pd loading have the lowest FOM (1.20 RIU^{-1}), this comparison reveals that Pd location can have a significant impact on the FOM by maximizing RIS while minimizing the effect of broadening. The LSPR plots for individual samples, as described in Table 1, in different RI can be found in Figure S8.

The effect of Pd distribution on RIS was further probed by comparing the octopodal Au seeds with tip-to-tip dimensions of 65.5 ± 2.5 and 85.9 ± 2.8 nm, respectively, to their corresponding Au−Pd heterostructures, with their structural and compositional features as well as optical properties summarized in Table S3. The plots for individual samples described in Table S3 can be found in Figures S9 and S10. As expected, the larger Au octopods had a further red shifted LSPR maximum (610 nm for tip-to-tip: 100.6 ± 2.4 nm *vs* 561 and 585 nm for 65.5 ± 2.5 and 85.9 ± 2.8 nm, respectively; all dispersed in water: RI = 1.3334), consistent with the size dependence of the LSPR.[14] The LSPR maxima of the Pd-tipped Au octopods were red shifted relative to their seeds, regardless of Pd loading. In contrast, the LSPR maxima of the Au@Pd octopods were within a few nm of the LSPR maxima of their seeds. Interpretation of these findings is aided by simulations presented later. Again, the Pd-tipped Au octopods with the largest loading (20.9% Pd) had the largest RIS (273 nm/RIU). This finding further supports the importance of Pd location in achieving high RIS.

The importance of Pd localization is also evident when comparing these structures to AuPd octopods of similar size and symmetry but where the Pd is alloyed with Au rather than creating a nanoscale heterostructure. Summarized in Table 1 are the previously reported optical properties of AuPd alloy octopods of similar dimensions and initial LSPR position.[9] Although the exact Pd loading for these structures was not reported, subsequent experiments using similar precursor ratios yielded structures with 5−15 at. % Pd.[23] These structures were chosen due to the dependence of RIS on the initial LSPR position.[24] Their RIS span 271 to 392 nm/RIU. For comparison, the Pd-tipped Au octopods with 20% Pd loading grown from 100.6 nm seeds have a RIS of 409 nm/RIU and a FOM of 1.71 RIU^{-1}, both of which are greater than the alloy AuPd octopods.

FDTD Simulations. To corroborate the experimental data and gain greater depth of understanding, FDTD simulations of octopodal models with different bimetallic distributions were conducted in which the far-field scattering behaviors of these structures were investigated in backgrounds of different RIs. The models included Au octopods, Pd-tipped Au octopods, and Au@Pd octopods with the background RI varied between 1.3334 and 1.4772 to simulate the experimental surroundings. The structural and compositional features of the models and the resulting optical properties are summarized in Table S4 and Figure S11. Figure 5A shows selectively this information for Au octopods with a tip-to-tip dimension of 100 nm (similar to NPs shown in Figure S2C) and those with approximately 20

https://doi.org/10.1021/acs.jpcc.1c02907
J. Phys. Chem. C 2021, 125, 11262−11270

A

Growth mode	Pd loading (at. %)	RIS (nm RIU^{-1})	FWHM (nm)	FOM (RIU^{-1})	λ_0 (nm)
Au	0	282	92	3.07	626
Pd-tip	20.2	322	144	2.24	656
Au@Pd	20	333	175	1.90	635

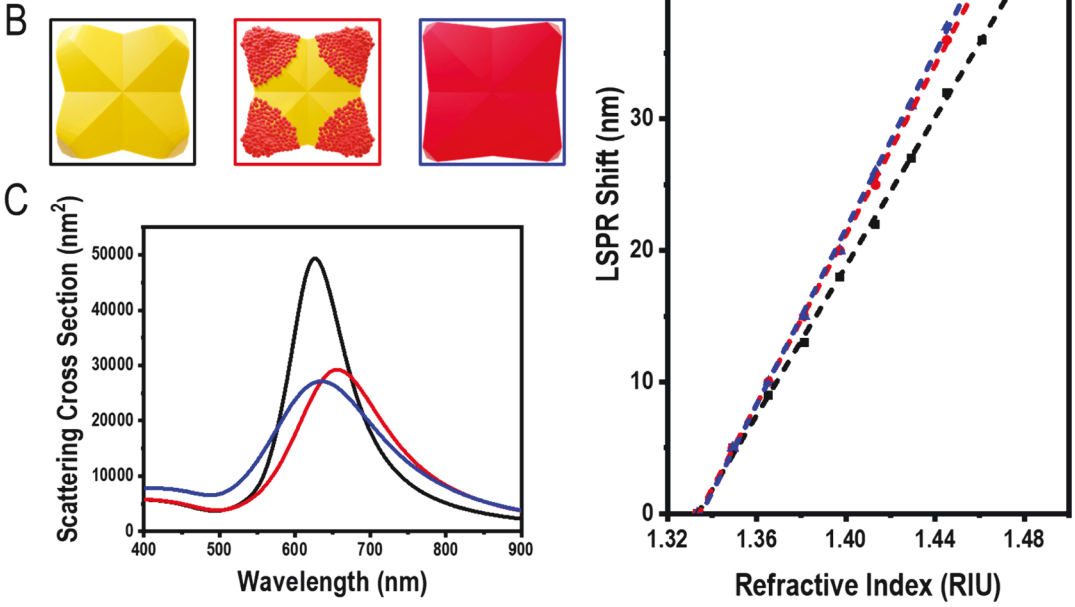

Figure 5. (A) Summary of the structural, compositional, and optical properties of the different models used for FDTD numerical simulations. (B) Models used for FDTD simulations viewed down the C_4 axis with the (black box) all-Au, (red box) Pd-tipped Au, and (blue box) Au@Pd octopods shown with the (C) corresponding plot of the far-field scattering of the models. (D) Plot of LSPR shift *vs* RI of the models with (black trace) Au, (red trace) Pd-tipped Au, and (blue trace) Au@Pd octopods present.

at. % Pd loaded at their tips or as a core@shell architecture (models shown in Figure 5B and similar to NPs shown in Figures 1D and 2D, respectively). The simulated spectra and RIS are presented in Figure 5C,D, respectively.

The Au octopod has a simulated RIS of 282 nm/RIU with an initial (RI of media = 1.3334) LSPR at 626 nm (Figure 5), which matches well with the experimental results of 275 nm/RIU and initial (water environment) LSPR at 610 nm (Figure 4). A slight red shift of the simulated LSPR may be from sharper edges in the model compared to the real NPs.[25] The narrower LSPR band in the simulation can be attributed to the idealized model, which does not suffer from ensemble broadening arising from size and structural heterogeneity in the experimental sample (Figure S12).[15,26] The good agreement between experiment and simulation establishes the Au octopod model as a reasonable platform to build the different Au−Pd heterostructures from.

The simulated spectrum of the Pd-tipped Au octopod in RI = 1.3334 is shown in Figure 5C and is red-shifted by 30 nm and broadened, with a FWHM increase of 52 nm, compared to the Au octopod model. A boost in RIS by 40 nm/RIU compared to the Au octopod model is achieved (Figure 5D). These observations are consistent with the experimental results, but the magnitude of the red shift and boost in RIS are less than the experimental system as the model gave a RIS of 322 nm/RIU and an initial LSPR maximum at 656 nm, whereas the RIS of the experimental system was 409 nm/RIU with an LSPR maximum at 694 nm. These differences, however, could be attributed to the sharpness of the features present in the model. It is well-documented that sharp features in branched plasmonic NPs lead to a red shift in the LSPR maximum.[6,25,27] The model simplified the island-like features to 5 nm diameter domes; however, the reality of the system is that the Pd islands are not domes, but ellipsoid-like structures with varying sizes that are randomly distributed around the branch tips (Figure S13). The change of shape of the islands between the experiment and the model, in addition to the greater uniformity present in the model, likely leads to a blue shifted and narrower LSPR compared to the experimental system. This blue shifted LSPR is likely the reason for the lower RIS of the model than that in the experimental system because the more red shifted the LSPR maximum is, typically, the higher the RIS.[24] Similar to the experimental system, increasing the Pd loading at the branch tips red shifts and broadens the modeled LSPR compared to the Au octopod model (Figure S14). In addition, as the Pd loading increased, so did the RIS, where the Pd-tipped Au octopod with the highest Pd loading simulated of 25.3% Pd loading had a RIS of 327 nm/RIU. The simultaneous increase in RIS and broadening of the LSPR in the simulations corroborates the trends observed through the experiment.

To simulate the Au@Pd octopods, a model consisting of an octopodal Au core and non-uniform Pd shell was built to capture the experimental observation of tip sharpening with Pd deposition (Figure S15A). This model failed to capture the experimental data precisely, likely due to unidentified heterogeneities in the experimental Pd shell; however, the trends present in the simulations provide useful insights. Namely, the Au@Pd sample gave a RIS of 244 nm/RIU experimentally, but the Au@Pd model with sharp branch tips (Figure S15A) gave a RIS of 333 nm/RIU. This drastic difference between experiment and simulation indicates that

https://doi.org/10.1021/acs.jpcc.1c02907
J. Phys. Chem. C 2021, 125, 11262−11270

some architectural feature from the experiment is unaccounted for in the model. To gain insights, a model of the same Pd loading but with a conformal Pd shell of uniform thickness was examined (Figure S15B). The model produced a RIS of 316 nm/RIU, closer to the experiment but still much higher than the experiment. Comparing the LSPR of the two core@shell models (RI = 1.3334), the model with the conformal Pd shell displayed a blue shifted LSPR maximum and narrower LSPR (Figure S16). Still, both models gave a broadened LSPR compared to the all-Au model. Additionally, the Au@Pd octopod simulations demonstrate the lowest FOM values of the models analyzed in this work. These simulations, despite differences from the experiment, support that a core@shell Au@Pd nanostructure does not provide the ideal Pd distribution on account of greater broadening with less red-shifting compared to the Pd-tipped system.

Taken together, the ideal Au−Pd octopods may be ones with single sharp Pd domains epitaxially capping each Au tip. This system would be advantageous with its localized Pd domains providing the benefits of boosted RIS without the broadening inherent in the Pd-tipped Au octopods stemming from the distribution of Pd islands around the tip. However, synthetic efforts have yet to achieve such selective metal deposition.

CONCLUSIONS

In summary, Au−Pd heterostructures were synthesized, and their optoelectronic properties were examined to identify the importance of Pd distribution on RIS. The localization of Pd around LSPR hotspots of branched Au NPs, as in the Pd-tipped Au octopod system, is critical in maximizing RIS. Larger loadings boost the RIS further, with an RIS of over 400 nm/RIU recorded. At the same time, the experimental findings indicate that increased Pd broadens linewidths, which must be balanced so as to not lower the FOM. FDTD simulations support the experimental trends, and also put emphasis on the overall sharpness of branch tips. Thus, in designing future plasmonic nanocrystals with high RIS, this work demonstrates the critical need to load material with low spectral dispersion around the LSPR hotspots of the system. In doing so, systems with boosted RIS and enhanced functionality can be achieved without compromising linewidth, pushing the sensing community beyond the Au standard.

ASSOCIATED CONTENT

Supporting Information

The Supporting Information is available free of charge at https://pubs.acs.org/doi/10.1021/acs.jpcc.1c02907.

Additional experimental information, model descriptions, electron microscopy images, and additional RIS experiments (PDF)

AUTHOR INFORMATION

Corresponding Author

Sara E. Skrabalak − *Department of Chemistry, Indiana University—Bloomington, Bloomington, Indiana 47405, United States;* orcid.org/0000-0002-1873-100X; Email: sskrabal@indiana.edu

Authors

Zachary J. Woessner − *Department of Chemistry, Indiana University—Bloomington, Bloomington, Indiana 47405, United States*

Alexander N. Chen − *Department of Chemistry, Indiana University—Bloomington, Bloomington, Indiana 47405, United States*

Complete contact information is available at: https://pubs.acs.org/10.1021/acs.jpcc.1c02907

Author Contributions

Z.J.W. and S.E.S. were responsible for the design of experiments. Z.J.W. was responsible for the synthesis and characterization of NPs and FDTD simulations detailed in this work. A.N.C. was responsible for STEM−EDS elemental mapping and TEM imaging for the different Au−Pd heterostructures studied. The manuscript was written through contributions of all authors. All authors have given approval to the final version of the manuscript.

Notes

The authors declare no competing financial interest.

ACKNOWLEDGMENTS

This work was supported by the Research Corporation for Science Advancement (Frontiers in Research Excellence Award) and the US National Science Foundation (NSF CHE 1904499 and 1602476). All authors acknowledge support from the Indiana University and Indiana University's Electron Microscopy Center and Nanoscale Characterization Facility for access to instrumentation.

REFERENCES

(1) Willets, K. A.; Van Duyne, R. P. Localized Surface Plasmon Resonance Spectroscopy and Sensing. *Annu. Rev. Phys. Chem.* **2007**, *58*, 267−297.

(2) Camden, J. P.; Dieringer, J. A.; Zhao, J.; Van Duyne, R. P. Controlled Plasmonic Nanostructures for Surface-Enhanced Spectroscopy and Sensing. *Acc. Chem. Res.* **2008**, *41*, 1653−1661.

(3) Mayer, K. M.; Hafner, J. H. Localized Surface Plasmon Resonance Sensors. *Chem. Rev.* **2011**, *111*, 3828−3857.

(4) Park, J.-E.; Lee, Y.; Nam, J.-M. Precisely Shaped, Uniformly Formed Gold Nanocubes with Ultrahigh Reproducibility in Single-Particle Scattering and Surface-Enhanced Raman Scattering. *Nano Lett.* **2018**, *18*, 6475−6482.

(5) Rodríguez-Lorenzo, L.; Álvarez-Puebla, R. A.; Pastoriza-Santos, I.; Mazzucco, S.; Stéphan, O.; Kociak, M.; Liz-Marzán, L. M.; García de Abajo, F. J. Zeptomol Detection Through Controlled Ultrasensitive Surface-Enhanced Raman Scattering. *J. Am. Chem. Soc.* **2009**, *131*, 4616−4618.

(6) Smith, J. D.; Woessner, Z. J.; Skrabalak, S. E. Branched Plasmonic Nanoparticles with High Symmetry. *J. Phys. Chem. C* **2019**, *123*, 18113−18123.

(7) Amendola, V.; Pilot, R.; Frasconi, M.; Maragò, O. M.; Iatì, M. A. Surface Plasmon Resonance in Gold Nanoparticles: a Review. *J. Phys.: Condens. Matter* **2017**, *29*, 203002.

(8) Rodal-Cedeira, S.; Montes-García, V.; Polavarapu, L.; Solís, D. M.; Heidari, H.; La Porta, A.; Angiola, M.; Martucci, A.; Taboada, J. M.; Obelleiro, F.; et al. Plasmonic Au@Pd Nanorods with Boosted Refractive Index Susceptibility and SERS Efficiency: A Multifunctional Platform for Hydrogen Sensing and Monitoring of Catalytic Reactions. *Chem. Mater.* **2016**, *28*, 9169−9180.

(9) DeSantis, C. J.; Skrabalak, S. E. Size-Controlled Synthesis of Au/Pd Octopods with High Refractive Index Sensitivity. *Langmuir* **2012**, *28*, 9055−9062.

(10) Ng, K. C.; Lin, F.-C.; Yang, P.-W.; Chuang, Y.-C.; Chang, C.-K.; Yeh, A.-H.; Kuo, C.-S.; Kao, C.-R.; Liu, C.-C.; Jeng, U.-S.; et al. Fabrication of Bimetallic Au−Pd−Au Nanobricks as an Archetype of Robust Nanoplasmonic Sensors. *Chem. Mater.* **2018**, *30*, 204−213.
(11) Sugawa, K.; Tahara, H.; Yamashita, A.; Otsuki, J.; Sagara, T.; Harumoto, T.; Yanagida, S. Refractive Index Susceptibility of the Plasmonic Palladium Nanoparticle: Potential as the Third Plasmonic Sensing Material. *ACS Nano* **2015**, *9*, 1895−1904.
(12) Smith, A. F.; Harvey, S. M.; Skrabalak, S. E.; Weiner, R. G. Engineering High Refractive Index Sensitivity Through the Internal and External Composition of Bimetallic Nanocrystals. *Nanoscale* **2016**, *8*, 16841−16845.
(13) Kadkhodazadeh, S.; Nugroho, F. A. A.; Langhammer, C.; Beleggia, M.; Wagner, J. B. Optical Property−Composition Correlation in Noble Metal Alloy Nanoparticles Studied with EELS. *ACS Photonics* **2019**, *6*, 779−786.
(14) Chang, C.-C.; Wu, H.-L.; Kuo, C.-H.; Huang, M. H. Hydrothermal Synthesis of Monodispersed Octahedral Gold Nanocrystals with Five Different Size Ranges and Their Self-Assembled Structures. *Chem. Mater.* **2008**, *20*, 7570−7574.
(15) Smith, A. F.; Weiner, R. G.; Skrabalak, S. E. Symmetry-Dependent Optical Properties of Stellated Nanocrystals. *J. Phys. Chem. C* **2016**, *120*, 20563−20571.
(16) Huglin, M. B. *Light Scattering from Polymer Solutions*; Academic Press: London, U.K., 1972.
(17) Johnson, P. B.; Christy, R. W. Optical Constants of the Noble Metals. *Phys. Rev. B: Solid State* **1972**, *6*, 4370−4379.
(18) Palik, E. D. *Handbook of Optical Constants of Solids*; Academic Press: London, U.K., 1998; Vol. *3*.
(19) le Roux, C. J.; Kriek, R. J. A Detailed Spectrophotometric Investigation of the Complexation of Palladium(II) with Chloride and Bromide. *Hydrometallurgy* **2017**, *169*, 447−455.
(20) Yang, T.-H.; Peng, H.-C.; Zhou, S.; Lee, C.-T.; Bao, S.; Lee, Y.-H.; Wu, J.-M.; Xia, Y. Toward a Quantitative Understanding of the Reduction Pathways of a Salt Precursor in the Synthesis of Metal Nanocrystals. *Nano Lett.* **2017**, *17*, 334−340.
(21) Yang, T.-H.; Gilroy, K. D.; Xia, Y. Reduction Rate as a Quantitative Knob for Achieving Deterministic Synthesis of Colloidal Metal Nanocrystals. *Chem. Sci.* **2017**, *8*, 6730−6749.
(22) Chen, H.; Kou, X.; Yang, Z.; Ni, W.; Wang, J. Shape- and Size-Dependent Refractive Index Sensitivity of Gold Nanoparticles. *Langmuir* **2008**, *24*, 5233−5237.
(23) Quintanilla, M.; Kuttner, C.; Smith, J. D.; Seifert, A.; Skrabalak, S. E.; Liz-Marzán, L. M. Heat generation by branched Au/Pd nanocrystals: influence of morphology and composition. *Nanoscale* **2019**, *11*, 19561−19570.
(24) Miller, M. M.; Lazarides, A. A. Sensitivity of Metal Nanoparticle Surface Plasmon Resonance to the Dielectric Environment. *J. Phys. Chem. B* **2005**, *109*, 21556−21565.
(25) Smith, A. F.; Weiner, R. G.; Bower, M. M.; Dragnea, B.; Skrabalak, S. E. Structure versus Composition: A Single-Particle Investigation of Plasmonic Bimetallic Nanocrystals. *J. Phys. Chem. C* **2015**, *119*, 22114−22121.
(26) Sherry, L. J.; Chang, S.-H.; Schatz, G. C.; Van Duyne, R. P.; Wiley, B. J.; Xia, Y. Localized Surface Plasmon Resonance Spectroscopy of Single Silver Nanocubes. *Nano Lett.* **2005**, *5*, 2034−2038.
(27) Cai, J.; Raghavan, V.; Bai, Y. J.; Zhou, M. H.; Liu, X. L.; Liao, C. Y.; Ma, P.; Shi, L.; Dockery, P.; Keogh, I.; et al. Controllable Synthesis of Tetrapod Gold Nanocrystals with Precisely Tunable Near-Infrared Plasmon Resonance Towards Highly Efficient Surface Enhanced Raman Spectroscopy Bioimaging. *J. Mater. Chem. B* **2015**, *3*, 7377−7385.

https://doi.org/10.1021/acs.jpcc.1c02907
J. Phys. Chem. C 2021, 125, 11262−11270